## PAPER

# Synthesis of magnetic NiFe$_2$O$_4$/g-C$_3$N$_4$ heterojunction photocatalysts for boosting dye degradation performance under visible-light irradiation†

Loan Thi To Nguyen, [a] Anh Thi Tu Duong,[a] Nguyen Duc Bui,[a] Viet Thi Mai Ngo,[a] Hai Quang Nguyen,[a] Hang Thi Thuy Nguyen,[b] Giang Thanh Tran[c] and Thuan Van Tran *[c]

Water pollution from dyes in wastewater is a critical global issue, as these stable organic dyes resist biodegradation, posing serious threats to aquatic ecosystems. To address this situation, advanced photocatalysts have been developed. Here, NiFe$_2$O$_4$/g-C$_3$N$_4$ was synthesized for the photocatalytic degradation of Rhodamine B (RhB) dye in the presence of H$_2$O$_2$ and visible light. Physicochemical analysis results showed NiFe$_2$O$_4$ nanoparticles dispersed in the g-C$_3$N$_4$ matrix, with an upward trend in the saturation magnetization of CNF$x$ as NiFe$_2$O$_4$ content rose. The surface area of CNF30 was 62.3 m$^2$ g$^{-1}$, outperforming both NiFe$_2$O$_4$ (23.2 m$^2$ g$^{-1}$) and g-C$_3$N$_4$ (48.5 m$^2$ g$^{-1}$). NiFe$_2$O$_4$/g-C$_3$N$_4$ could be reused up to four cycles, and efficiently catalyzed the degradation of nearly 98% RhB dye, showing a decreased rate of up to 95% COD. Through scavenger studies, the main role of ˙OH was demonstrated. Therefore, highly efficient and recyclable NiFe$_2$O$_4$/g-C$_3$N$_4$ can be a potential photocatalyst for degradation of dyes.

## 1. Introduction

The expansion of industries and growing population have intensified environmental and health concerns, especially with the extensive use of synthetic dyes across various sectors, which significantly contributes to water pollution.[1] Many of these dyes are either slow to biodegrade or are entirely non-biodegradable, making them challenging to treat using conventional waste-water methods.[1,2] Additionally, their toxicity can severely disrupt the metabolism of living organisms, posing risks such as mutagenicity and carcinogenicity.[3,4] Without timely intervention, these pollutants may cause irreversible harm to ecosystems, underscoring the need for sustainable and effective solutions to mitigate these environmental hazards.

Currently, the variety of available wastewater treatment processes provides a robust basis for selecting the most effective methods for specific pollutants. Advanced physical techniques

$^a$Faculty of Chemistry, Thai Nguyen University of Education, Thai Nguyen 240000, Vietnam

$^b$Faculty of Automotive and Power Machinery Engineering, Thai Nguyen University of Technology, Thai Nguyen 24000, Vietnam

$^c$Institute of Applied Technology and Sustainable Development, Nguyen Tat Thanh University, 298-300A Nguyen Tat Thanh, District 4, Ho Chi Minh City 755414, Vietnam. E-mail: tranvt@ntt.edu.vn; tranuv@gmail.com; Fax: +84-028-39-404-759; Tel: +84-028-3941-1211

† Electronic supplementary information (ESI) available. See DOI: https://doi.org/10.1039/d4na00694a

such as sedimentation, ion exchange, and membrane filtration, for instance, achieve high-efficiency removal of organic and inorganic solids from water.[5] Additionally, bioremediation of textile wastewater using different organisms, e.g., bacteria, fungi, algae, enzymes, and mixed cultures under aerobic and anaerobic conditions has proven particularly effective as it decomposes organic contaminants and converts dissolved organic matter into biomass.[6] Furthermore, physicochemical treatments, including coagulation–flocculation, activated carbon-based adsorption, photocatalysis, electrochemical methods, and advanced oxidation processes, have also shown strong performance in removing pollutants.[7] Notably, among these, advanced oxidation processes are extensively regarded as the most effective for degrading dye molecules in wastewater.[8]

Over the last two decades, two-dimensional graphitic carbon nitride (g-C$_3$N$_4$) has emerged as one of the most prominent photocatalysts for physicochemical applications due to its favorable thermochemical stability, cost-effectiveness, ease of synthesis, narrow band gap energy (2.9 eV), and abundant charge carriers within its tri-$s$-triazine and triazine units.[9–11] However, the photocatalytic performance of g-C$_3$N$_4$ is hindered by obstacles such as a low surface area, rapid recombination of photogenerated electron–hole pairs, and limited absorption efficiency ($\leq$450 nm).[12] To overcome these issues, researchers have explored modifications with elements such as sulfur, phosphorus, potassium, and sodium, which have shown to enhance the photocatalytic activity of g-C$_3$N$_4$.[13] Additionally,

combining with other semiconductors, such as magnetic spinel ferrite, offers a promising approach due to its ability to broaden the absorption spectrum, reduce bandgap energy, improve thermochemical stability, and increase charge separation, thereby boosting photocatalytic efficiency.[9] Nickel ferrite ($NiFe_2O_4$), with band gaps of 1.5–1.7 eV and greater absorption within the visible spectrum, serves as a beneficial component to enhance photocatalytic applications.[14] Thus, the presence of $NiFe_2O_4$ in binary semiconductors helps form Z-scheme or S-scheme heterojunctions in minimizing charge recombination and enhancing photocatalytic activity.

Numerous studies on $NiFe_2O_4$/g-$C_3N_4$ have demonstrated high effectiveness in photodegrading various pollutants in water, underscoring its strong potential as a key material for wastewater treatment.[15–17] The $NiFe_2O_4$/g-$C_3N_4$ composite has photodegradation potential to degrade a broad range of pharmaceutical substances, such as ofloxacin, cephalexin, and tetracycline hydrochloride, along with harmful dyes such as methylene blue, methyl orange, and rhodamine B.[15,18–21] Remarkably, $NiFe_2O_4$/g-$C_3N_4$ achieved removal rates 30–50% higher than those obtained with individual components (g-$C_3N_4$ and $NiFe_2O_4$). However, moderate degradation rate and long treatment duration using the $NiFe_2O_4$/g-$C_3N_4$ composite might be the major drawbacks in these studies. Importantly, $NiFe_2O_4$/g-$C_3N_4$ stability and recyclability as well as the photocatalytic mechanism for RhB degradation were not clarified insightfully. Necessary tests such as chemical oxygen demand to monitor the amount of oxygen in the treated water were rarely conducted.

Here, several improvements in experimental conditions are implemented to enhance the RhB photodegradation performance using the $NiFe_2O_4$/g-$C_3N_4$ composite, offering a deeper analysis compared to prior studies. These novel points may distinguish this research on RhB elimination using $NiFe_2O_4$/g-$C_3N_4$ composites. These advancements aim to distinguish our findings on RhB degradation with this composite. Firstly, unlike previous studies relying on direct solar irradiation, which varies in photon intensity, the photodegradation process was achieved by irradiation using a stable photon source of LED light, ensuring consistent photon energy throughout the process.[21,22] Secondly, a chemical oxygen demand (COD) experiment for measuring the total organic matter after the reaction was conducted. Thirdly, a plausible and detailed mechanism for RhB photodegradation by the $NiFe_2O_4$/g-$C_3N_4$ composite was proposed through incorporating recent insights on semiconductor heterojunction mechanisms. This addressed the gap left by prior studies,[21] which did not confirm whether the mechanism was a type-II heterojunction or an S-scheme. Our proposed mechanism provides a more comprehensive understanding, confirming that the S-scheme mechanism best describes the photodegradation process.

## 2. Materials and methods

### 2.1. Synthesis of g-$C_3N_4$

First, 10 g of urea was added into a ceramic crucible and capped carefully. The solid was calcined at 500 °C with a heating rate of 5 °C min$^{-1}$ for 2 h to obtain g-$C_3N_4$. Afterward, the g-$C_3N_4$ solid

was ground finely, washed with 0.1 M $HNO_3$ solution, and distilled water many times. Finally, the sample was dried at 110 °C to obtain pure g-$C_3N_4$.

### 2.2. Synthesis of $NiFe_2O_4$

In this study, urea acted as a fuel for the combustion method. First, 8.0 g urea was dissolved in 20 mL distilled water. 5.82 g $Ni(NO_3)_2 \cdot 6H_2O$ and 16.2 g of $Fe(NO_3)_3 \cdot 9H_2O$ were added into this solution. The mixture was magnetically stirred on a heating machine at 70 °C for 4 h. The sample was dried in an oven, and then transferred into a ceramic crucible. The solid was calcined at 500 °C for 3 h to obtain the $NiFe_2O_4$ sample. The chemical equation for the reaction can be described as follows:

$$3Ni(NO_3)_2 + 6Fe(NO_3)_3 + 20(NH_2)_2CO \rightarrow 3NiFe_2O_4 + 32N_2 + 20CO_2 + 40H_2O$$
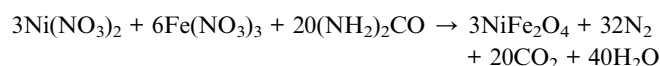
### 2.3. Synthesis of the $NiFe_2O_4$/g-$C_3N_4$ composite

Fig. 1 shows the synthesis procedure of the $NiFe_2O_4$/g-$C_3N_4$ composite. In detail, 0.01 g of the synthesized $NiFe_2O_4$ was elaborately mixed with 0.09 g of g-$C_3N_4$, and transferred into a ceramic crucible. Then, the mixture was calcined at 450 °C for 2 h. The solid was washed with distilled water, and dried to obtain the $NiFe_2O_4$/g-$C_3N_4$ material, denoted as CNF10. The number "10" means that the weight of $NiFe_2O_4$ accounted for 10% of the total weight of $NiFe_2O_4$ and g-$C_3N_4$. Similarly, composite samples with 20% $NiFe_2O_4$ (CNF20) and 30% $NiFe_2O_4$ (CNF30) were prepared by adjusting the proportions accordingly. The synthesis of these samples was conducted similar to that of the CNF10 sample.
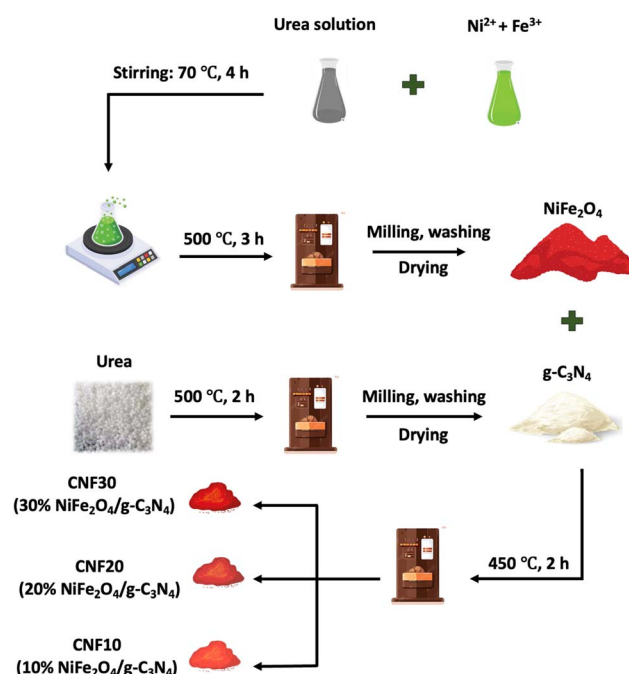


Fig. 1 The synthesis of g-$C_3N_4$, $NiFe_2O_4$, and $NiFe_2O_4$/g-$C_3N_4$ composite.

## 2.4. Photocatalytic experiments

For a typical run, 0.1 g of the catalyst was added into 100 mL RhB dye solution (20 mg L$^{-1}$). The adsorption was carried out under dark conditions for 90 min to reach equilibrium. Note that after every 30 min, the solution was sampled (2 mL) and centrifuged to monitor the UV-Vis absorption spectra. After 90 min of adsorption, a volume of 30% H$_2$O$_2$ was added into the solution to obtain an [H$_2$O$_2$] of 0.2 M. The mixture was stirred under illumination using LED light. Every 30 min, the solution was sampled with 2 mL to monitor the absorbance. The maximum absorbance of RhB was determined at approximately 500 nm.

## 3. Results and discussion

### 3.1. Characterization

**3.1.1. Crystallinity.** Fig. 2a illustrates the XRD pattern of g-C$_3$N$_4$, NiFe$_2$O$_4$, and CNF$x$ ($x$ = 10, 20, 30). For g-C$_3$N$_4$, two typical peaks at 2-theta of 13.0° and 27.65°were observed, which are assigned to the (100) and (002) planes. These signals may relate to the in-plane structural interlayer stacking of the aromatic system of g-C$_3$N$_4$ (JCPDS No. 87-1526).[23,24] For NiFe$_2$O$_4$, the intensive peaks at 30.3°, 35.7°, 37.4°, 43.5°, 57.4°, and 63.2° are indexed to the (220), (311), (222), (400), (511), and (440) crystal planes, respectively (JCPDS No. 00-003-0875).[25] However, in the pattern of NiFe$_2$O$_4$, less intense peaks are observed, which may be explained by the presence of iron or nickel oxide phases in the sample, indicating it is not a completely pure sample.[15] Most patterns of CNF$x$ ($x$ = 10, 20, 30) show the inheritance of

peaks from g-C$_3$N$_4$ and NiFe$_2$O$_4$. However, the decrease in intensity of the two peaks at planes (100) and (002) of CNF$x$ is attributed to the anchoring of NiFe$_2$O$_4$ on sheets of g-C$_3$N$_4$.[24,26,27] This finding demonstrates the successful synthesis of CNF$x$ composites with pure lattices.

**3.1.2. Surface chemistry.** Fig. 2b illustrates the surface chemistry of g-C$_3$N$_4$, NiFe$_2$O$_4$, and CNF$x$ ($x$ = 10, 20, 30) composites. For g-C$_3$N$_4$, the peak around 800 cm$^{-1}$ corresponds to the breathing mode of the tri-$s$-triazine unit.[28] Vibrations in the range of 1200–1650 cm$^{-1}$ are attributed to the stretching of C–N heterocycles.[29] A peak at 3175 cm$^{-1}$ is associated with adsorbed free water molecules or uncondensed N–H stretching vibrations.[30] For NiFe$_2$O$_4$, peaks at 500–600 cm$^{-1}$ correspond to metal–oxygen vibrations.[19,29] NiFe$_2$O$_4$ also shows additional peaks at 1000–1700 cm$^{-1}$, assigned by the stretching and bending of C=C or C–N bonds. These impurities likely result from using urea as a combustion agent in the synthesis process. The spectra of CNF$x$ ($x$ = 10, 20, 30) composites inherit peaks from both g-C$_3$N$_4$ and NiFe$_2$O$_4$. A noticeable increase in the intensity of the metal–oxygen vibration peaks is observed when the NiFe$_2$O$_4$ grafted on g-C$_3$N$_4$ sheet is increased.

**3.1.3. Magnetization.** The magnetic hysteresis loops of NiFe$_2$O$_4$ and CNF$x$ ($x$ = 10, 20, 30) indicate several magnetic properties, including saturation magnetization ($M_s$), coercivity ($H_c$), and remnant magnetization ($M_r$) as observed in Fig. 2c. Considering the shape of the magnetic hysteresis loops, both NiFe$_2$O$_4$ and CNF$x$ composites are soft ferromagnetic materials. NiFe$_2$O$_4$ exhibited an $M_s$ value of 32.86 emu g$^{-1}$. This value gradually decreased as the NiFe$_2$O$_4$ content in CNF$x$ composites
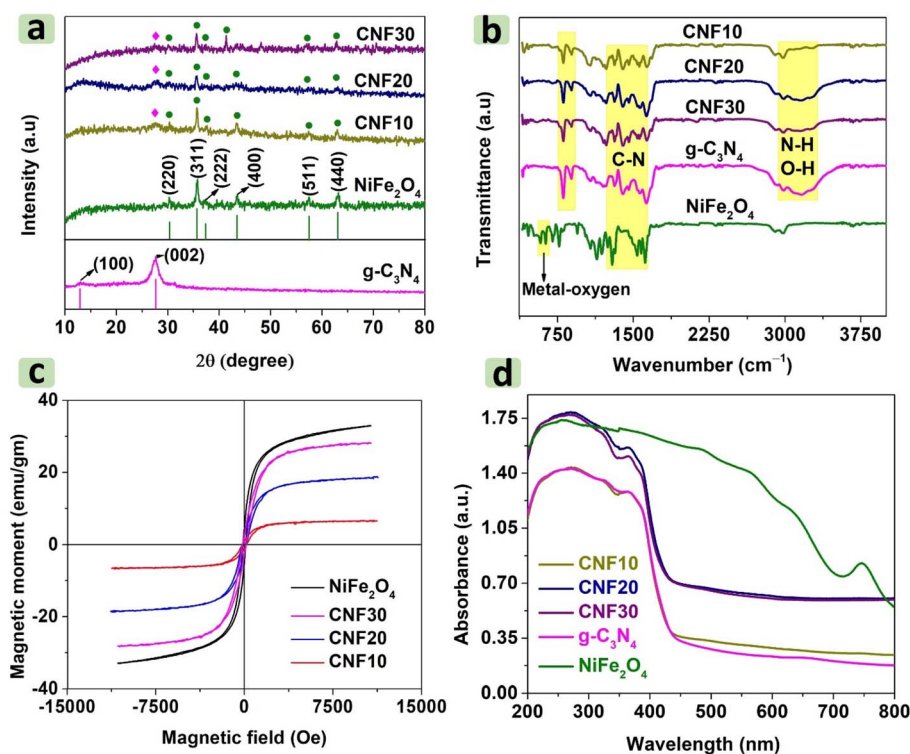


**Fig. 2** The XRD patterns (a), FTIR spectra (b), magnetization curves (c) and UV-Vis DRS spectra (d) of g-C$_3$N$_4$, NiFe$_2$O$_4$, and CNF$x$ ($x$ = 10, 20, 30).
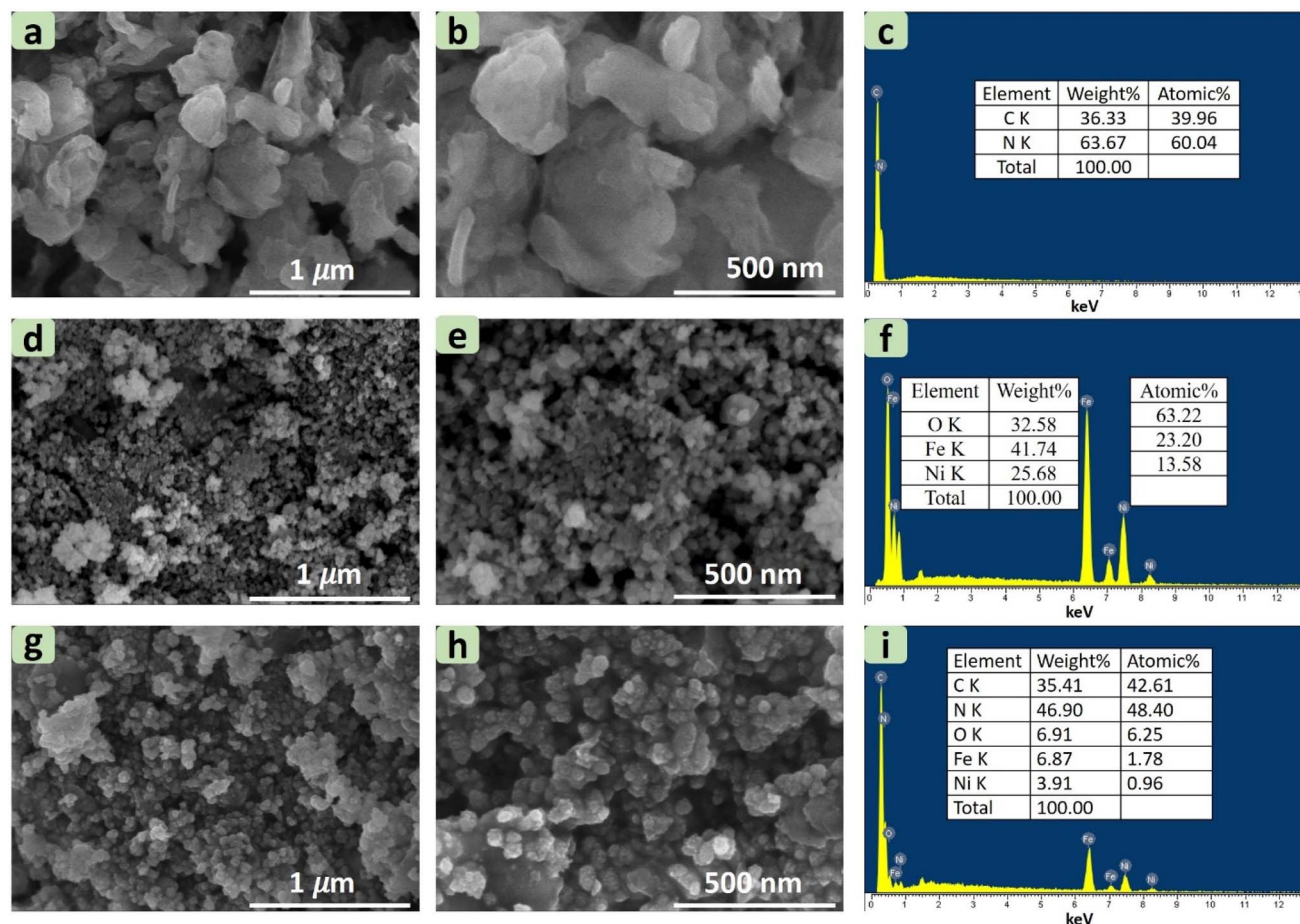
Fig. 3   SEM images of g-$C_3N_4$ (a and b) and EDX analysis (c). SEM images of $NiFe_2O_4$ (d and e) and EDX analysis (f). SEM images of CNF30 (g and h) and EDX analysis (i).

decreased from 30% to 10%, resulting in $M_s$ values from 28.09 emu $g^{-1}$ to 6.52 emu $g^{-1}$ as summarized in Table S1 in the ESI† document. The reduction of $M_s$ values is attributed to the combination with the non-magnetic material g-$C_3N_4$, significantly lowering the magnetic saturation of the CNF$x$ composites. However, previous studies often reported higher magnetic saturation values of $NiFe_2O_4$, typically at 40–50 emu $g^{-1}$.[31–33] This discrepancy may result from $NiFe_2O_4$ impurities due to the use of urea as a combustion agent in the synthesis process.

**3.1.4. Optical properties.** The UV-visible diffuse reflectance spectrum (DRS) analysis helps in better understanding the optical properties and light absorption of photocatalysts. Fig. 2d illustrates the UV-Vis DRS spectra of g-$C_3N_4$, $NiFe_2O_4$, and CNF$x$ ($x$ = 10, 20, 30). Firstly, g-$C_3N_4$ strongly absorbs in the wavelength below 450 nm, rendering it inactive in the visible light region. This result is consistent with other research studies on synthesizing g-$C_3N_4$, where the illumination absorption is attributed to the $\pi \to \pi^*$ and $n \to \pi^*$ transitions in the tri-$s$-triazine or tri-$s$-heptazine units.[34–36] Meanwhile, the absorption band of $NiFe_2O_4$ was observed in the range of 450–700 nm (visible light region). Therefore, combining g-$C_3N_4$ and $NiFe_2O_4$ forms a $NiFe_2O_4$/g-$C_3N_4$ composite that can be excited by photon irradiation in the UV-Vis region.

To access the separation efficiency of photo-generated electron–hole ($e^-$–$h^+$) pairs of g-$C_3N_4$ and CNF30 composite, photoluminescence (PL) spectra at a wavelength range of 400–600 nm were recorded. According to Fig. S1,† g-$C_3N_4$ has an emission peak at around 438 nm, compared with the 434 nm of CNF30. Moreover, the PL intensity of g-$C_3N_4$ is considerably decreased in comparison to that of CNF30, indicating the migration of $e^-$–$h^+$ pairs between g-$C_3N_4$ and $NiFe_2O_4$. Therefore, the $e^-$–$h^+$ recombination rate of CNF30 decreased, likely increasing its photocatalytic performance.

**3.1.5. Morphology and chemical composition.** Fig. 3 reveals the morphology of g-$C_3N_4$, $NiFe_2O_4$, and CNF30 composite. According to Fig. 3a and b, g-$C_3N_4$ exhibits an uneven distribution of sheet sizes, ranging from 50 to 500 nm, with a flake-like morphology. $NiFe_2O_4$ nanoparticles, on the other hand, are slightly concentrated and distributed below 50 nm in size, with a spherical shape as shown in Fig. 3d and e. Notably, the CNF30 composite shows densely grafted $NiFe_2O_4$ nanoparticles on the surface of the g-$C_3N_4$ sheet, indicating the successful decoration of g-$C_3N_4$ with $NiFe_2O_4$ nanoparticles. This observation aligns with several previous reports.[37,38]

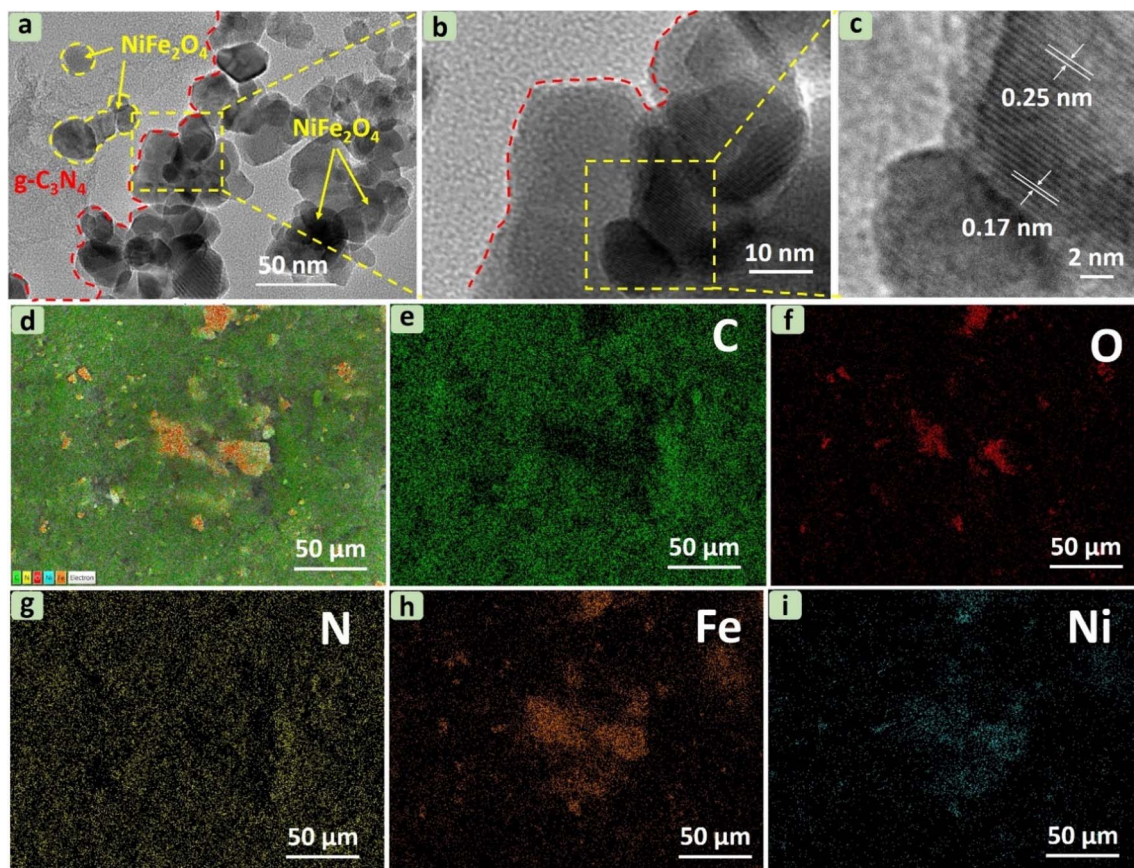The elemental composition and percentage of elements in g-$C_3N_4$, $NiFe_2O_4$, and CNF30 composite are presented through

**Fig. 4** HR-TEM (a–c) and EDS mapping (d–i) of CNF30.

EDX analysis in Fig. 3. The obtained data confirm the presence of main elements in g-$C_3N_4$, $NiFe_2O_4$, and CNF30. Notably, the double calcination of g-$C_3N_4$ led to a change in the C/N ratio in the g-$C_3N_4$ and CNF30 samples. In pure g-$C_3N_4$, the atomic ratio of C/N was 0.67, compared with 0.88 of CNF30. This finding indicates a decrease in the nitrogen content after two successive heating at 500 °C and 450 °C due to the deamination process.[26]

The internal structure of g-$C_3N_4$ in Fig. S2† reflects the thin flat shape of irregular 2D nanosheets as reported previously.[39] For the composite, HRTEM images in Fig. 4a and b show $NiFe_2O_4$ particles with an average size of about 50 nm embedded in g-$C_3N_4$ nanosheets in CNF30, agreeable with previous studies.[19,21] Decoration of $NiFe_2O_4$ by g-$C_3N_4$ at the edge is also observed in Fig. S3.† Two distinct lattice fringes at 0.17 nm (440) and 0.25 nm (311) in Fig. 4c are attributable to lattices of $NiFe_2O_4$, suggesting the presence of $NiFe_2O_4$ in the CNF30 heterojunction.[40] Moreover, EDS mapping of CNF30 in Fig. 4d–i shows good distribution of C, O, N, Fe and Ni in CNF30, which was consistent with the EDX analysis results.

**3.1.6. Surface area and porosity.** From the $N_2$ adsorption–desorption isotherm curves in Fig. 5a, it is evident that g-$C_3N_4$, $NiFe_2O_4$, and CNF30 samples exhibit type III with H3-type



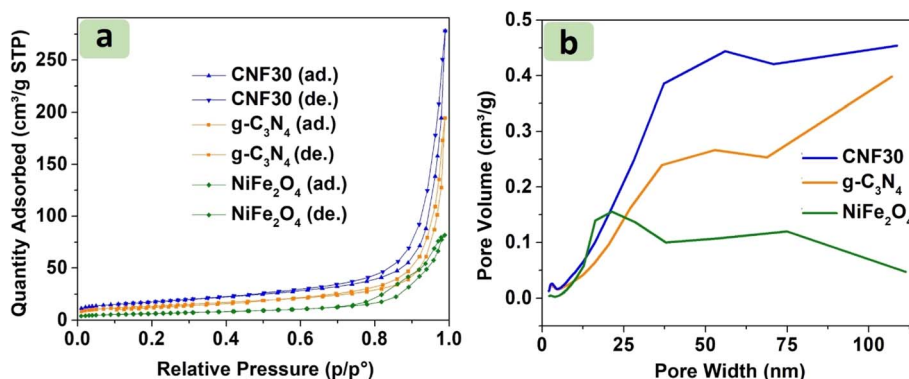**Fig. 5** $N_2$ adsorption–desorption isotherm curves (a) and BJH adsorption d$V$/d log($w$) pore volume (b) of g-$C_3N_4$, $NiFe_2O_4$, and CNF30.
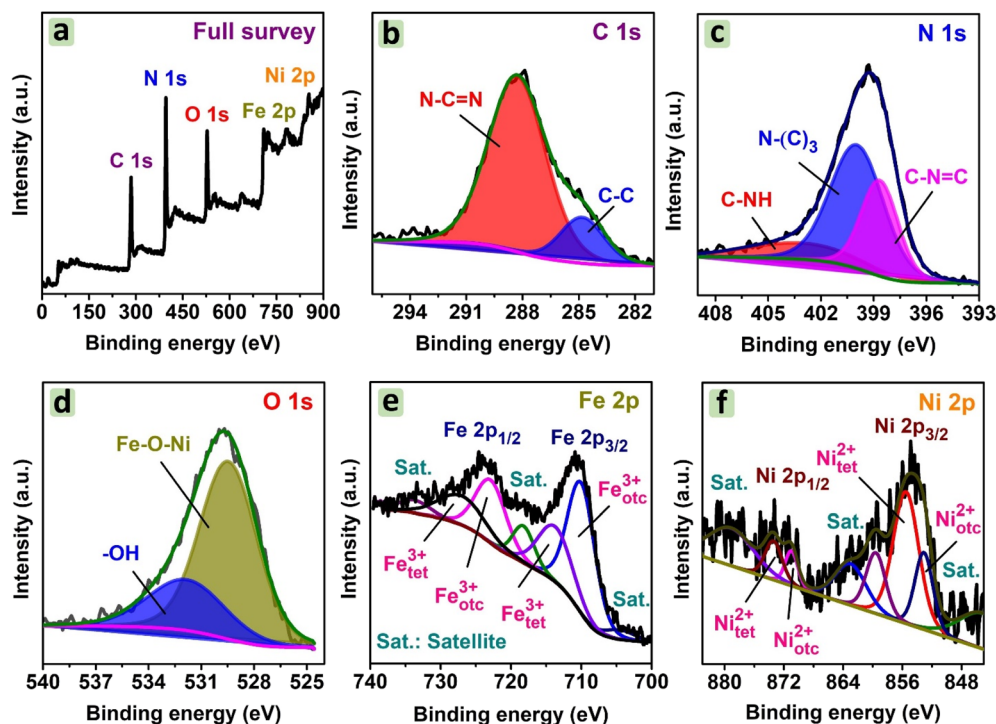
Fig. 6 XPS analysis of CNF30: (a) full survey, (b) C1s, (c) N1s, (d) O1s, (e) Fe 2p, and (f) Ni 2p.

hysteresis loops, indicating the reversible isotherms and the presence of wedge-shaped pores. The pore size distribution in Fig. 5b and the values in Table S1† show that the pore sizes of g-$C_3N_4$, $NiFe_2O_4$, and CNF30 are 30.7, 22.3, and 31.8 nm, respectively. Additionally, the BET surface area of CNF30 was found at 62.3 $m^2$ $g^{-1}$, higher than that of g-$C_3N_4$ at 48.5 $m^2$ $g^{-1}$ and $NiFe_2O_4$ at 23.2 $m^2$ $g^{-1}$. In other words, the surface area of CNF30 was approximately equal to the sum of the surface areas of g-$C_3N_4$ and $NiFe_2O_4$. This indicates the decoration of g-$C_3N_4$ sheets with $NiFe_2O_4$ nanoparticles without significant defects to the overall porous structure. The slightly lower surface area of CNF30 compared to the sum surface areas of the components can be attributed to the deposition of $NiFe_2O_4$ nanoparticles into the pores of g-$C_3N_4$, leading to some pore blockage and a slight reduction in surface area. Additionally, the second calcination of g-$C_3N_4$ and $NiFe_2O_4$ at 450 °C also partially affected the porous features.

**3.1.7. Elemental valence states.** The elemental valence states of CNF30 were analyzed using the XPS spectrum (Fig. 6). According to Fig. 6a, CNF30 is constituted of five main elements: C, N, O, Fe, and Ni, which are commensurate with the observation in EDX and TEM mapping analyses. Fig. 6b shows deconvoluted C1s peaks at 284.8 eV and 288.3 eV, corresponding to C–C and N–C=N bonds. Meanwhile, Fig. 6c shows three deconvoluted N1s peaks at 398.7 eV, 400.0 eV, and 403.4 eV, corresponding to C–N=C, N–(C)$_3$, and C–NH groups. These bonds belong to g-$C_3N_4$, as reported previously.[41,42] For O1s, Fig. 6d suggests the presence of oxygen–metal bonds in $NiFe_2O_4$ particles at 529.5 eV. Another peak at 532.0 eV can be hydroxyl groups, which resulted from water adsorbed in CNF30.[21] For Fe

2p, the spectrum in Fig. 6e highlights two regions including Fe 2p$_{3/2}$ at 710.2 eV and 714.2 eV, and Fe 2p$_{1/2}$ at 723.3 eV and 727.8 eV. Moreover, the deconvolution indicates two $Fe^{3+}$ states in the octahedral and tetrahedral sites.[43] Similarly, the deconvolution of Ni 2p$_{3/2}$ at 853.1 eV and 855.6 eV, and Ni 2p$_{1/2}$ at 871.0 eV and 873.5 eV can be observed in Fig. 6f.

**3.1.8. Photoelectrochemical properties.** In this study, electrochemical impedance spectroscopy (EIS) spectra of $NiFe_2O_4$ and CNF30 were examined to explore their photo-generated charge transfer performance with glassy carbon as the working electrode and 3 M KCl as the electrolyte solution. Fig. S4† reveals that the photochemical impedance of CNF30 was smaller than that of $NiFe_2O_4$. Moreover, based on the diameter of semicircles in Nyquist plots, charge transfer resistance ($R_{ct}$) values of $NiFe_2O_4$ and CNF30 were measured at 126.42 and 97.88 ohm, respectively. It should be understood that smaller charge transfer resistance facilitates charge transfer.[44] This result indicates that CNF30 likely enhanced carrier separation and electron transfer compared with $NiFe_2O_4$.

The cyclic voltammetric curves of $NiFe_2O_4$ and CNF30 at a scan rate of 50 mV $s^{-1}$ are shown in Fig. S5.† Both photocatalysts exhibited typical redox voltammogram loops. Moreover, specific capacitance ($C_p$) can be calculated as follows, (eqn (1)).[45]

$$C_p = \frac{1}{m \times (V_2 - V_1) \times k} \int_{V_1}^{V_2} I(V) \mathrm{d}V \tag{1}$$

where $m$ is the weight of the active material (g), $V$ is the potential, $I$ is the current (A), and $k$ is the scan rate of cyclic voltammetry (V $s^{-1}$). The integral part $\int_{V_1}^{V_2} I(V)\mathrm{d}V$ can be
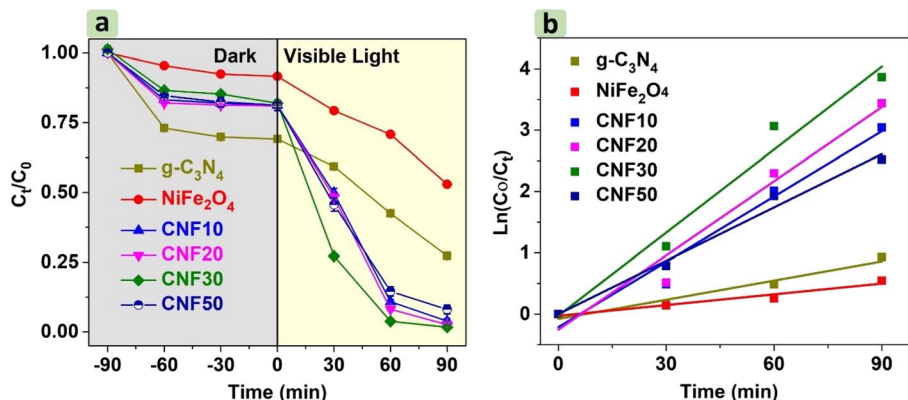
**Fig. 7** Photocatalytic degradation of RhB by g-C$_3$N$_4$, NiFe$_2$O$_4$, and CNF$x$ ($x$ = 10, 20, 30, 50) (a), and photodegradation kinetics fitted by the pseudo-first-order model (b).

calculated as the area of the cyclic voltammetric curve. Based on Fig. S5,† the specific capacitance ($C_p$) values were measured at 61.48 and 83.70 F g$^{-1}$ for NiFe$_2$O$_4$ and CNF30, respectively. Decoration of NiFe$_2$O$_4$ with g-C$_3$N$_4$ might increase the number of electrochemical active sites and lower band gap, accelerating ionic diffusion and improving specific capacitance.[46] As a result, CNF30 proved to be a potential photocatalyst for capturing and retaining the charge under visible-light irradiation.

### 3.2. Photocatalytic degradation

**3.2.1. Effect of NiFe$_2$O$_4$ loading ratio.** Fig. 7a shows the photocatalytic degradation of RhB by g-C$_3$N$_4$, NiFe$_2$O$_4$, and CNF$x$ ($x$ = 10, 20, 30, 50). Prior to photodegradation, batch experimental setups were placed in the dark for 90 min to achieve adsorption–desorption equilibrium. The results show that g-C$_3$N$_4$ has the highest elimination efficiency at 30.2%, compared to NiFe$_2$O$_4$ nanoparticles at 7.9% and CNF$x$ ($x$ = 10, 20, 30, 50) at 15.6–18.7%. This phenomenon is understandable since adsorption was primarily influenced by surface area, pore types, and interactions. The CNF$x$ composites achieved better RhB adsorption efficiency compared to NiFe$_2$O$_4$ nanoparticles due to its higher surface area as shown in Table S1.† Moreover, g-C$_3$N$_4$ exhibited the highest adsorption efficiency, possibly due to effective π–π stacking interactions between the aromatic backbone of the dye molecule and the highly delocalized π-

conjugated system of g-C$_3$N$_4$.[47] In the CNF$x$ composites, the structure of the g-C$_3$N$_4$ sheet undergoes partial alteration due to double calcination. This alteration affects the aromatic structure of the g-C$_3$N$_4$ sheet, as mentioned in EDX analysis, where differences in the C/N ratio were observed between the pure g-C$_3$N$_4$ sheet and the g-C$_3$N$_4$ within the composite.

The photolysis of RhB (without the catalyst) exhibited a minimal decline of nearly 5% in 90 min. The degradation efficiency of RhB by CNF30 showed the highest value at 97.9%, while CNF10 and CNF20 achieved photodegradation efficiencies of 95.2% and 96.8%, respectively. Increasing NiFe$_2$O$_4$ content (50%) did not lead to increased degradation efficiency of CNF50 since the value was found at 91.9%. The superiority of all CNF$x$ ($x$ = 10, 20, 30, 50) compared to g-C$_3$N$_4$ (60.6%) and NiFe$_2$O$_4$ (42.2%) was attributed to the formation of heterojunctions within the CNF$x$ composites, which led to efficient charge transfer.[48] The absorption of photon energy allowed the CNF$x$ heterojunctions to generate a large and stable number of electrons through the excitation process. These electrons moved to the conduction band more easily, reducing electron–hole recombination. Several studies also reported that the NiFe$_2$O$_4$/g-C$_3$N$_4$ composites offered better photodegradation efficiency against antibiotics and dyes compared to single photocatalysts.[19,29,49]

To clearly evaluate the kinetic degradation of RhB by g-C$_3$N$_4$, NiFe$_2$O$_4$, and CNF$x$ ($x$ = 10, 20, 30, 50), the pseudo-first-order
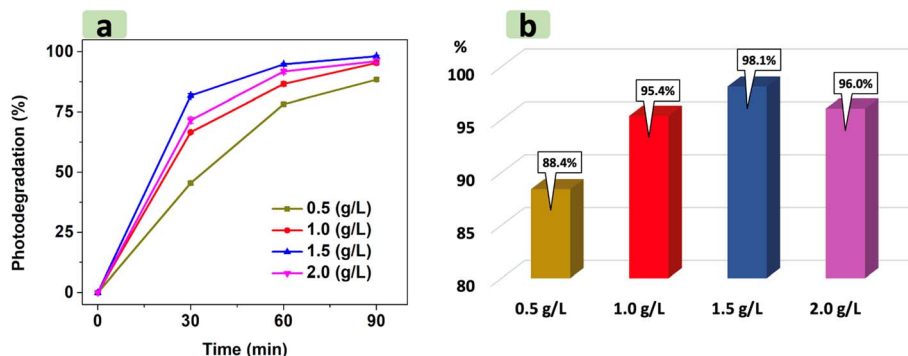


**Fig. 8** Effect of CNF30 dosage on RhB photocatalytic degradation (a), the RhB degradation percentage after 90 min at various dosages (b).
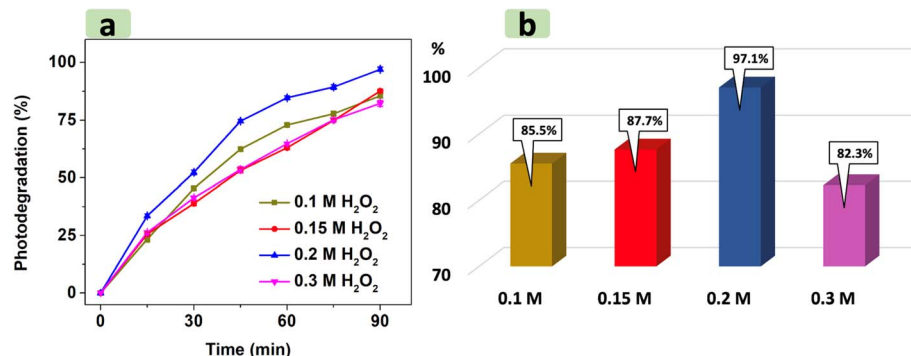
**Fig. 9** Effect of $H_2O_2$ concentration on RhB photocatalytic degradation under visible light (a), the RhB degradation percentage after 90 min at various $H_2O_2$ concentrations (b).

model was applied. Fig. 7b shows that all models for describing photodegradation are reliable, with $R^2$ values ranging from 0.93 to 0.96. Table S2† also reveals that CNF30 exhibits the highest reaction rate constant ($k_1$) at 0.045 min$^{-1}$. Due to its remarkable photodegradation efficiency and rate, CNF30 was chosen as the optimal catalyst for the photodegradation of RhB.

**3.2.2. Effect of dosage.** Fig. 8 illustrates the effect of the amount of CNF30 catalyst on RhB photodegradation. An increase in the quantity of CNF30 led to higher degradation efficiency. When the amount of CNF30 increased from 0.5 g L$^{-1}$ to 1.5 g L$^{-1}$, the photodegradation efficiency rose from 88.4% to 98.1%. This significant enhancement could be attributed to the increased formation of reactive oxygen species due to the higher availability of active sites on CNF30, which directly participated in the catalytic degradation of RhB.[50] As CNF30 was added from 1.5 g L$^{-1}$ to 2.0 g L$^{-1}$, however, a slight decrease in photodegradation efficiency from 98.1% to 96.0% was observed. A similar result was observed for the photodegradation of methyl orange by the g-C$_3$N$_4$/ZnO/Ag$_3$PO$_4$ composite and g-C$_3$N$_4$/CdO nanocomposite for degrading RhB.[51,52] This phenomenon can be explained using three prevailing reasons. Firstly, excessive CNF30 increased the turbidity of RhB solution, obstructing incident radiation and thus reducing dye degradation.[53,54] Secondly, an excessive amount of CNF30 might cause agglomeration, leading to a decrease in the surface area and active sites of CNF30.[51] Thirdly, the excess CNF30 in the solution led to the formation of Fe$^{2+}$ ion scavengers, which trap OH$^{\bullet}$ radicals, reducing the availability of these radicals for the photodegradation process.[55,56]

**3.2.3. Effect of [H$_2$O$_2$].** Hydrogen peroxide (H$_2$O$_2$) generates hydroxyl radicals for the photocatalytic reaction and prevents electron–hole recombination of the photocatalyst. As a result, the investigation of [H$_2$O$_2$] is important to obtain optimum degradation yield and reduce chemical cost. Here, the role of H$_2$O$_2$ in the RhB photodegradation is shown in Fig. S6.† Accordingly, the photocatalytic performance of g-C$_3$N$_4$, NiFe$_2$O$_4$ and CNF30 without H$_2$O$_2$ addition is very low, at below 30%. This result suggests that H$_2$O$_2$ played a vital role in creating OH radicals necessary for the RhB degradation reaction.

Fig. 9 illustrates that increasing H$_2$O$_2$ concentration from 0.1 M to 0.2 M increases photodegradation efficiency from

85.5% to 97.1%. This trend was attributed to the higher density of H$_2$O$_2$ in RhB solution, which acted as an effective scavenger by trapping electrons from the conduction band of CNF30 to create more hydroxyl radicals.[57] When H$_2$O$_2$ concentration exceeds the optimal level (0.2 M), however, the RhB photodegradation yield significantly declines to 82.3%. In addition to scavenging electrons, excessive H$_2$O$_2$ amount also generates hydroxyl ($^{\bullet}$OH) and hydroperoxyl ($^{\bullet}$OOH) radicals.[55,56,58] The reaction between these two radicals to form H$_2$O and O$_2$ may reduce the availability of radicals necessary for the photodegradation process.

**3.2.4. Effect of [RhB].** The effect of RhB concentration ([RhB]) on the photodegradation yield is illustrated in Fig. 10. When [RhB] varies between 20 and 25 mg L$^{-1}$, there is no significant alteration in RhB photodegradation of CNF30. As [RhB] increases from 25 mg L$^{-1}$ to 50 mg L$^{-1}$, however, the degradation efficiency significantly decreases from 96.6% to 44.5%. Wang et al.[59] also demonstrated that the RhB photodegradation efficiency of an activated biochar/potassium-doped g-C$_3$N$_4$ composite declined from nearly 99% to 78% when [RhB] increased from 50 mg L$^{-1}$ to 200 mg L$^{-1}$. This trend can be attributed to the unavailability of active sites on the surface of CNF30, as well as complex interactions between unreacted RhB molecules and radical species.[51]
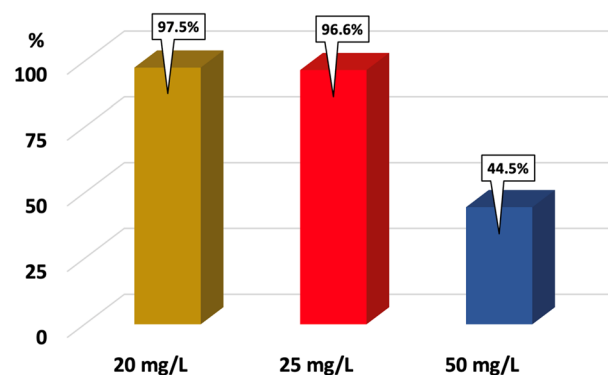


**Fig. 10** The effect of RhB initial concentration on the photodegradation efficiency of CNF30 (H$_2$O$_2$: 0.2 M, dose: 1.5 g L$^{-1}$).
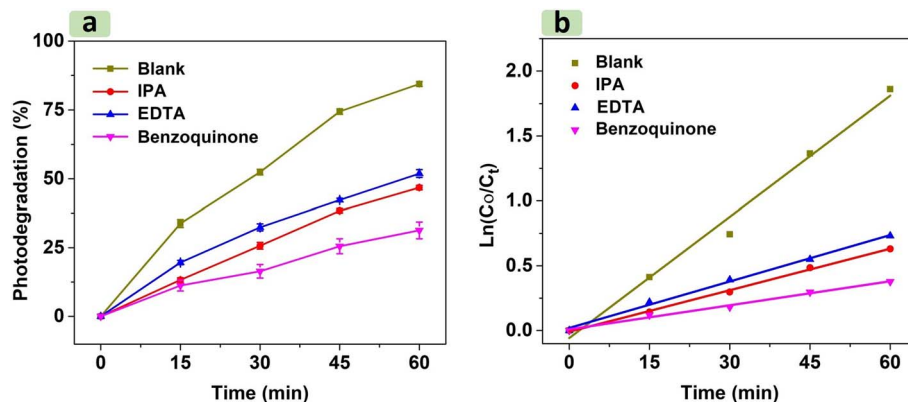
**Fig. 11** Trapping experiment of three radical scavengers in RhB photodegradation by CNF30 (a), kinetic photodegradation of the three radical scavengers (b).

**3.2.5. Scavenging experiments.** To investigate the involvement of radical species in RhB photodegradation, a scavenging experiment was run. Fig. 11a shows the trapping test conducted using three different scavengers: isopropyl alcohol (IPA), ethylenediaminetetraacetic acid disodium (EDTA), and benzoquinone (BQ). These scavengers were introduced into the reaction mixture to trap hydroxyl radicals ($^{\bullet}$OH), holes (h$^{+}$), and superoxide radicals ($^{\bullet}$O$_2^{-}$) during the photodegradation of RhB. In the presence of IPA, EDTA, and BQ, the photocatalytic degradation of RhB by CNF30 was 46.8%, 51.9%, and 31.3%, respectively, which were so far lower than that of the blank sample at 84.5%. Fig. 11b also indicates that the RhB degradation rate constants (0.006–0.012 min$^{-1}$) in the presence of scavengers were lower than that (0.031 min$^{-1}$) of the blank. Thus, these results suggest that radical species significantly affected the RhB photodegradation kinetics. The order of inhibition of the photodegradation efficiency was BQ ($^{\bullet}$O$_2^{-}$) > IPA ($^{\bullet}$OH) > EDTA (h$^{+}$).

**3.2.6. Plausible photocatalytic mechanisms.** To suggest a suitable mechanism for the photocatalytic process of CNF30, the energy potentials of the conduction band (CB) and valence band (VB) of the semiconductors can be calculated according to the following equations, eqn (2) and (3).[60]

$$E_{VB} = \chi - E_c + 0.5E_g \tag{2}$$

$$E_{CB} = E_{VB} - E_g \tag{3}$$

where $E_{CB}$ and $E_{VB}$ are the CB and VB potentials of the semiconductor, $\chi$ is the Mulliken electronegativity of the catalyst, $E_c$ stands for the energy of free electrons ($\sim$4.5 eV) on the hydrogen scale and $E_g$ represents the band-gap energy of the photocatalyst. The values of $\chi$ for NiFe$_2$O$_4$ and g-C$_3$N$_4$ are 5.85 eV[26,61] and 4.73 eV,[24] respectively.

For NiFe$_2$O$_4$ NPs, the calculated VB and CB edge positions are 2.19 and 0.51 V vs. NHE, respectively. For g-C$_3$N$_4$ microsheets, the calculated VB and CB edge positions are 1.71 and −1.25 V vs. NHE, respectively. The trapping experiment results show that ($^{\bullet}$OH), ($^{\bullet}$O$_2^{-}$) and (h$^{+}$) species participate in the RhB degradation. Evaluating the photocatalytic degradation of

CNF30 based on the type-II heterojunction mechanism reveals several drawbacks, suggesting that it is not suitable to explain the degradation of RhB or is not the main mechanism. After photon irradiation from an LED light, electron/hole pairs form. In a type-II heterojunction, electrons move from the CB of g-C$_3$N$_4$ to the CB of NiFe$_2$O$_4$ since the CB of g-C$_3$N$_4$ (−1.25 eV) is more negative than that of NiFe$_2$O$_4$ (0.51 V). Simultaneously, holes transfer from the VB of NiFe$_2$O$_4$ (2.19 V) to the VB of g-C$_3$N$_4$ (1.71 V) due to the higher positive VB of g-C$_3$N$_4$. However, at the CB of NiFe$_2$O$_4$ (0.51 V), the standard reduction potential (O$_2$/O$_2$$^{\bullet-}$) ($E_0$ = −0.33 V vs. NHE) is more negative than the CB of NiFe$_2$O$_4$; therefore, superoxide radicals cannot be created.[62] Furthermore, the standard oxidation potential (OH$^{-}$/HO$^{\bullet}$) ($E_0$ = +1.99 V vs. NHE) is also more positive than the VB of g-C$_3$N$_4$ (1.71 V); therefore, hydroxyl radicals cannot be created.[63] Due to these obstacles in the formation of hydroxyl and superoxide radicals, the type-II heterojunction mechanism is not the main mechanism in the degradation process.

On the other hand, the photocatalytic degradation of RhB through the S-scheme mechanism can explain the treatment process by CNF30 as illustrated in Fig. 12. After photon irradiation, g-C$_3$N$_4$ and NiFe$_2$O$_4$ semiconductors contact each other via Fermi level alignment. This electron migration leads to upward bending of g-C$_3$N$_4$ (positive) and downward bending of NiFe$_2$O$_4$ (negative).[15] This process generates inbuilt electric fields at the interface of the two semiconductors, coulombic repulsion, and band bending, which inhibit the transfer of electrons from the CB of g-C$_3$N$_4$ to that of NiFe$_2$O$_4$ as well as the transfer of holes from the VB of NiFe$_2$O$_4$ to that of g-C$_3$N$_4$ (in the type-II heterojunction path).[27] Consequently, the electrons with less negative charge at the CB of NiFe$_2$O$_4$ can combine with holes with less positive charge at the VB of g-C$_3$N$_4$. Next, the reduction reaction occurs to form O$_2$$^{\bullet-}$ at the highest energy potential of the CB of g-C$_3$N$_4$ (−1.25 V) due to the potential being more negative than the standard reduction potential (O$_2$/O$_2$$^{\bullet-}$ = −0.33 V). Simultaneously, the oxidation reaction to form HO$^{\bullet}$ occurs at the highest energy potential of the VB of NiFe$_2$O$_4$ (2.19 V) due to the potential being more positive than the standard oxidation potential (OH$^{-}$/HO$^{\bullet}$ = +1.99 V). Moreover,
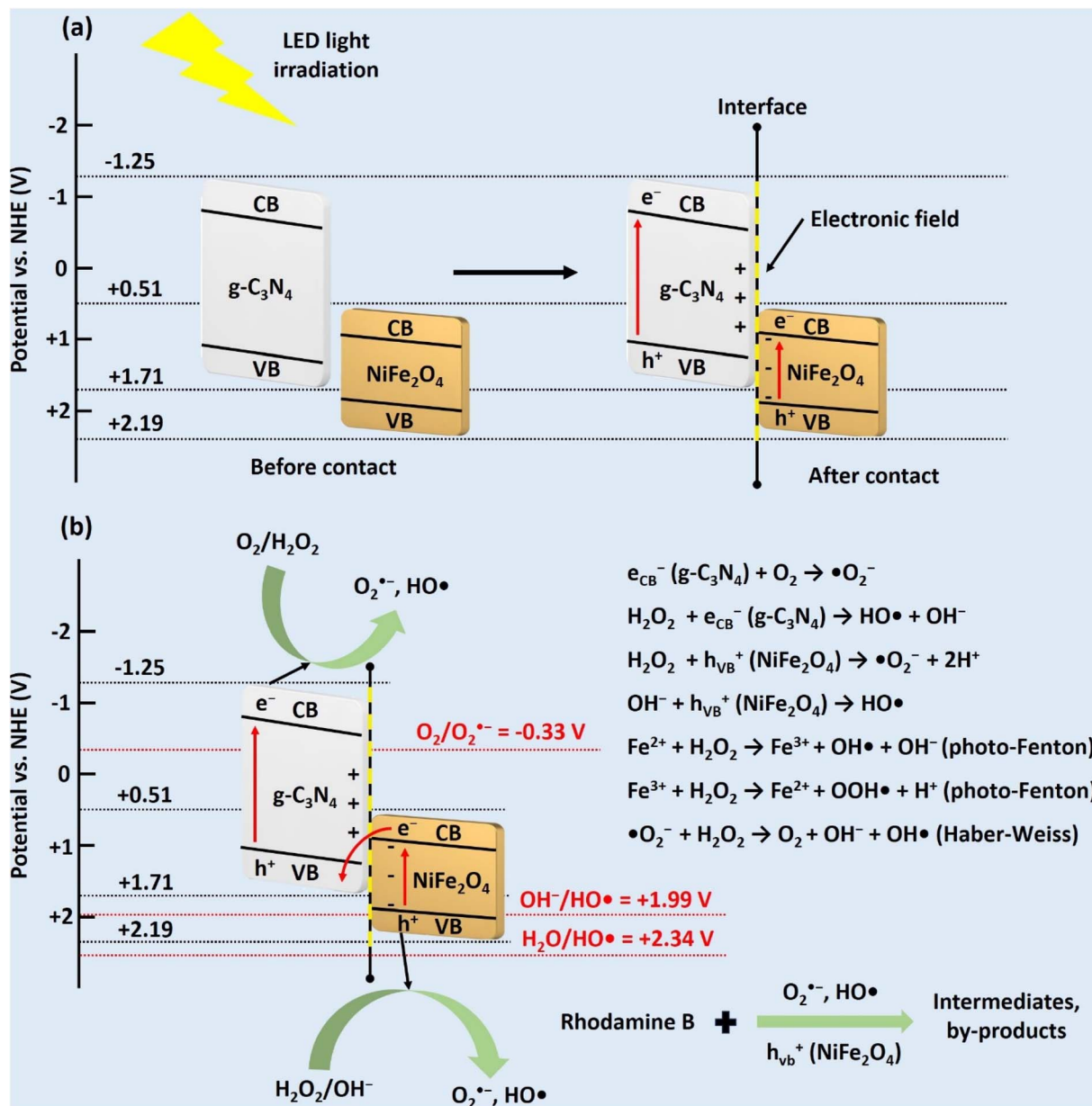
**Fig. 12** Proposed mechanism of RhB photodegradation by $NiFe_2O_4$/g-$C_3N_4$. After receiving photon energy, electric fields, coulombic repulsion, and band bending, which hinder type-II heterojunction and support the S-scheme mechanism (a). The RhB photodegradation process involves radical species (b).

the standard oxidation potential ($H_2O/HO^{\bullet}$ = +2.34 V) is higher than that of the VB of $NiFe_2O_4$; therefore, some holes may directly oxidize the RhB molecules.[64] Finally, the combination of the S-scheme mechanism and the scavenging experiment results can explain the photocatalytic degradation of RhB in the presence of the three radical species.

**3.2.7. Recyclability and chemical oxygen demand tests.** To demonstrate the practical potential of CNF30 for water treatment systems, a recyclability study was conducted. This experiment was carried out by washing CNF30 after using as a photocatalyst with ethanol and water many times to remove RhB molecules trapped in CNF30 pores. The recovered CNF30

was dried and used as a photocatalyst for the next cycle. According to Fig. 13a, CNF30 exhibits high recyclability with four cycles. After the 4th cycle, RhB was still degraded up to 91%, indicating that catalytic sites on CNF30 remained active. Moreover, the crystallinity of reused CNF30 was checked (Fig. S6†), showing that the major peaks for g-$C_3N_4$ at (002) and for $NiFe_2O_4$ at (220), (331), (222), (511) and (440) still remained. Thus, CNF30 achieved high recyclability and structural stability after the dye degradation experiments.

Chemical oxygen demand (COD) is a crucial parameter that indicates the amount of oxygen required to oxidize organic compounds in water. According to Fig. 13b, the COD value for
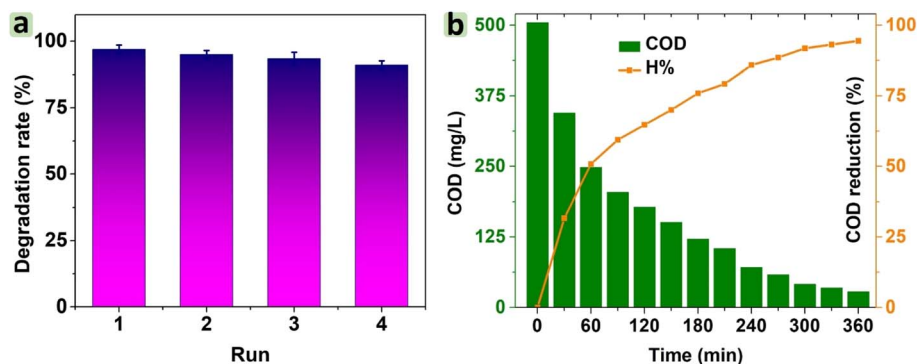
**Fig. 13** Recyclability test of CNF30 (a) and the percentage of COD reduction over time (b).

**Table 1**  A comparison of dye degradation performance of photocatalysts

| Photocatalyst | Type of dye pollutant | Degradation time (min) | Catalyst dosage ($g\ L^{-1}$) | Dye concentration ($mg\ L^{-1}$) | COD reduction rate (%) | $k_1$ ($1\ min^{-1}$) | Number of reuses | Degradation efficiency (%) At the 1st cycle | At the final cycle | Ref. |
|---|---|---|---|---|---|---|---|---|---|---|
| $NiFe_2O_4$/g-$C_3N_4$ | Rhodamine B | 90 | 1.0 | 20 | 95.0 | 0.045 | 4 | 98.0 | 91.0 | This study |
| $NiFe_2O_4$/(N,S) graphene oxide | Rhodamine B | 240 | 0.5 | 100 | 90.3 | 0.012 | 3 | 95.2 | 90.3 | 65 |
| Cellulose bead supported-$CoFe_2O_4$ | Rhodamine B | 60 | 0.4 | 40 | 85.6 | 0.089 | 5 | 99.5 | 78.0 | 66 |
| Alginate-$ZnCO_2O_4$ | Rhodamine B | 40 | 1.0 | 25 | 82.0 | 0.146 | 5 | 98.2 | 78.0 | 67 |
| $ZnCo_2O_4$/ N-doped g-$C_3N_4$ | Rhodamine B | 60 | 0.35 | 10 | 79.6 | 0.098 | 5 | 92.3 | 83.4 | 68 |
| $Zn_xMn_{1-x}Fe_2O_4$ | Rhodamine B | 180 | 1.0 | 20 | 80 | 0.006 | 4 | 95.3 | 80 | 69 |
| $Bi_2O_3$/BiOCl | Rhodamine B | 120 | 0.5 | 10 | 67.2 | 0.027 | 5 | 96.8 | 92.6 | 70 |
| MgO–Fe | Rhodamine B | 240 | 0.75 | 10 | 67.0 | 0.047 | — | 97.8 | — | 71 |
| Biosynthesized Ag@ZnO | Rhodamine B | 120 | 1.0 | 100 | 74.8 | 0.013 | — | 90 | — | 72 |
| Biosynthesized ZnO | Rhodamine B | 120 | 1.0 | 100 | 41.3 | — | — | 50 | — | 72 |

RhB degradation was 504.7 mg $L^{-1}$, and this value gradually decreased to 28.0 mg $L^{-1}$ after 360 min. A significant reduction in COD indicates the effective mineralization of RhB, implying that RhB could be largely broken down into smaller molecules or fragments. Moreover, the percentage of COD reduction increased to 94.5% after 360 min under visible light, suggesting that CNF30 was highly effective in degrading RhB. This result highlighted the potential of CNF30 for practical applications in wastewater treatment.

**3.2.8. Comparison study.** To assess the RhB degradation performance of $NiFe_2O_4$/g-$C_3N_4$ (CNF30) in this study compared with that of photocatalysts in other studies, a comparative table is summarized. According to Table 1, experimental conditions including degradation time, catalyst dosage, and dye concentration herein are relatively mild. Moreover, COD reduction rate using the CNF30/$H_2O_2$/visible light system was 95%, higher than that of photocatalytic systems in most studies surveyed so far (41.4–90.3%). The first-order rate constant is also higher than reported results. Although this work studied a moderate

number of cycles (four times), the degradation efficiency obtained was still very high (91%) at the final cycle. A majority of surveyed studies reported lower results (78–90.3%) at the final cycle. As a result, CNF30 with such good recyclability and efficiency may be a competitive photocatalyst for solving wastewater treatment issues.

## 4.   Conclusion

Here, $NiFe_2O_4$/g-$C_3N_4$ was synthesized and applied for the photocatalytic degradation of RhB dye. The morphological results revealed that $NiFe_2O_4$ nanoparticles were dispersed in the g-$C_3N_4$ matrix. There was an upward trend in the saturation magnetization (6.5–28.1 emu $g^{-1}$) of CNFx with $NiFe_2O_4$ amount (10–30%). The surface area of CNF30 was 62.3 $m^2\ g^{-1}$, significantly higher than that of $NiFe_2O_4$ and g-$C_3N_4$. Nearly 98% RhB dye was degraded with a decrease level of 95% COD using the CNF30/$H_2O_2$/visible light system. The highest first-order kinetic rate was 0.045 $min^{-1}$ for the reaction catalyzed by CNF30. The scavenger studies threw light on the important

role of $\cdot O_2^-$, $\cdot OH$, and $h^+$ species. After the 4th cycle, CNF30 still exhibited high photocatalytic activity at an efficiency of 91% and high stability. Therefore, $NiFe_2O_4/g$-$C_3N_4$ can be suggested as a potential photocatalyst for degradation of dyes.

## Ethical statement

The authors declare that the manuscript has not been published anywhere or submitted to another journal. The manuscript is not currently being considered for publication in any another journal. All authors have been personally and actively involved in substantive work leading to the manuscript, and will hold themselves jointly and individually responsible for its content. The research does not involve any human participants and/or animals.

## Data availability

The data supporting this article have been included as part of the ESI.†

## Code availability

The authors declare that software application or custom code supports their published claims and complies with field standards.

## Author contributions

Loan Thi To Nguyen: conceptualization, investigation, project administration, supervision; Anh Thi Tu Duong: investigation formal analysis, resources; Nguyen Duc Bui: investigation, formal analysis; Viet Thi Mai Ngo: investigation, data curation; Hai Quang Nguyen: validation, visualization; Hang Thi Thuy Nguyen: validation, data curation; Giang Thanh Tran: writing – original draft, validation; Thuan Van Tran: writing – original draft, writing review & editing, methodology, supervision. All authors read and approved the final manuscript.

## Conflicts of interest

The authors declare that there are no conflicts of interest.

## Acknowledgements

## References

1 A. Tkaczyk, K. Mitrowska and A. Posyniak, *Sci. Total Environ.*, 2020, **717**, 137222.

2 A. Srivastava, R. M. Rani, D. S. Patle and S. Kumar, *J. Chem. Technol. Biotechnol.*, 2022, **97**, 26–41.

3 G. T. Tran, N. T. H. Nguyen, N. T. T. Nguyen, T. T. T. Nguyen, D. T. C. Nguyen and T. V. Tran, *Environ. Chem. Lett.*, 2023, **21**, 2417–2439.

4 M. Köktürk, *Sci. Total Environ.*, 2022, **852**, 158473.

5 S. F. Ahmed, M. Mofijur, S. Nuzhat, A. T. Chowdhury, N. Rafa, M. A. Uddin, A. Inayat, T. M. I. Mahlia, H. C. Ong, W. Y. Chia and P. L. Show, *J. Hazard. Mater.*, 2021, **416**, 125912.

6 V. Gopinath, S. M. Kamath, S. Priyadarshini, Z. Chik, A. A. Alarfaj and A. H. Hirad, *Biomed. Pharmacother.*, 2022, **146**, 112492.

7 V. Ganthavee and A. P. Trzcinski, *J. Ind. Eng. Chem.*, 2023, **126**, 20–35.

8 H. M. Solayman, M. A. Hossen, A. Abd Aziz, N. Y. Yahya, K. H. Leong, L. C. Sim, M. U. Monir and K.-D. Zoh, *J. Environ. Chem. Eng.*, 2023, **11**, 109610.

9 T. Garg, Renu, J. Kaur, P. Kaur, Nitansh, V. Kumar, K. Tikoo, A. Kaushik and S. Singhal, *Chem. Eng. J.*, 2022, **443**, 136441.

10 B. Zhu, L. Zhang, B. Cheng and J. Yu, *Appl. Catal., B*, 2018, **224**, 983–999.

11 A. Kumar, A. Kumar, G. Sharma, A. H. Al-Muhtaseb, M. Naushad, A. A. Ghfar, C. Guo and F. J. Stadler, *Chem. Eng. J.*, 2018, **339**, 393–410.

12 W. Muhammad, W. Ali, M. A. Khan, F. Ali, A. Zada, M. Z. Ansar and P.-S. Yap, *J. Environ. Chem. Eng.*, 2024, **12**, 113409.

13 J. Wang and S. Wang, *Coord. Chem. Rev.*, 2022, **453**, 214338.

14 S. Singh, A. K. Atri, I. Qadir, S. Sharma, U. Manhas and D. Singh, *ACS Omega*, 2023, **8**, 6302–6317.

15 S. K. Sharma, A. Kumar, G. Sharma, M. Naushad, M. Ubaidullah and A. García-Peñas, *Colloids Surf., A*, 2022, **654**, 129968.

16 R. R. M. Silva, L. A. M. Ruotolo and F. G. E. Nogueira, *Chem. Eng. J.*, 2023, **476**, 146621.

17 D. Sun, J. Mao, L. Cheng, X. Yang, H. Li, L. Zhang, W. Zhang, Q. Zhang and P. Li, *Chem. Eng. J.*, 2021, **418**, 129417.

18 G. Zhao, J. Ding, F. Zhou, X. Chen, L. Wei, Q. Gao, K. Wang and Q. Zhao, *Chem. Eng. J.*, 2021, **405**, 126704.

19 S. Liu, A. Zada, X. Yu, F. Liu and G. Jin, *Chemosphere*, 2022, **307**, 135717.

20 G. Gebreslassie, P. Bharali, U. Chandra, A. Sergawie, P. K. Baruah, M. R. Das and E. Alemayehu, *Appl. Organomet. Chem.*, 2019, **33**, e5002.

21 B. Palanivel, C. Ayappan, V. Jayaraman, S. Chidambaram, R. Maheswaran and A. Mani, *Mater. Sci. Semicond. Process.*, 2019, **100**, 87–97.

22 P. Mishra, L. Acharya and K. Parida, *Mater. Today: Proc.*, 2021, **35**, 281–288.

23 C. Li, M. Li, S. Yin, L. Zeng and L. Zhang, *J. Alloys Compd.*, 2021, **861**, 157986.

24 M. Moradi, B. Kakavandi, A. Bahadoran, S. Giannakis and E. Dehghanifard, *Sep. Purif. Technol.*, 2022, **285**, 120313.

25 S. A. Hassanzadeh-Tabrizi, *J. Photochem. Photobiol., A*, 2021, **418**, 113398.

26 I. F. Waheed, M. A. Hamad, K. A. Jasim and A. J. Gesquiere, *Diamond Relat. Mater.*, 2023, **133**, 109716.

27 R. Acharya, S. Pati and K. Parida, *J. Mol. Liq.*, 2022, **357**, 119105.

28 B. Palanivel, C. Hu, M. Shkir, S. AlFaify, F. A. Ibrahim, M. S. Hamdy and A. Mani, *Colloid Interface Sci. Commun.*, 2021, **42**, 100410.

29 B. Palanivel, M. Shkir, T. Alshahrani and A. Mani, *Diam. Relat. Mater.*, 2021, **112**, 108148.

30 K. Qi, A. Zada, Y. Yang, Q. Chen and A. Khataee, *Res. Chem. Intermed.*, 2020, **46**, 5281–5295.

31 H. A. El-Sabban, A. H. Mady, M. A. Diab, S. Y. Attia and S. G. Mohamed, *Surf. Interfaces*, 2024, **44**, 103798.

32 S. Ravi Kumar, G. Vishnu Priya, B. Aruna, M. K. Raju, D. Parajuli, N. Murali, R. Verma, K. Mujasam Batoo, R. Kumar and P. V. Lakshmi Narayana, *Inorg. Chem. Commun.*, 2022, **136**, 109132.

33 P. Kumar, S. Pathak, A. Singh, H. Khanduri, Kuldeep, K. Jain, J. Tawale, L. Wang, G. A. Basheed and R. P. Pant, *J. Alloys Compd.*, 2021, **887**, 161418.

34 X. Zeng, S. Shu, Y. Meng, H. Wang and Y. Wang, *Chem. Eng. J.*, 2023, **456**, 141105.

35 V. Vinesh, M. Preeyanghaa, T. R. N. Kumar, M. Ashokkumar, C. L. Bianchi and B. Neppolian, *Environ. Res.*, 2022, **207**, 112112.

36 F. Hasanvandian, M. Moradi, S. Aghaebrahimi Samani, B. Kakavandi, S. Rahman Setayesh and M. Noorisepehr, *Chemosphere*, 2022, **287**, 132273.

37 C. Lu, J. Wang, D. Cao, F. Guo, X. Hao, D. Li and W. Shi, *Mater. Res. Bull.*, 2023, **158**, 112064.

38 S. Solgi, M. S. Seyed Dorraji, S. F. Hosseini, M. H. Rasoulifard, I. Hajimiri and A. Amani-Ghadim, *Sci. Rep.*, 2021, **11**, 19339.

39 K. Sun, J. Shen, Q. Liu, H. Tang, M. Zhang, S. Zulfiqar and C. Lei, *Chin. J. Catal.*, 2020, **41**, 72–81.

40 X. Li, L. Wang, L. Zhang and S. Zhuo, *Appl. Surf. Sci.*, 2017, **419**, 586–594.

41 S. Gong, Z. Jiang, S. Zhu, J. Fan, Q. Xu and Y. Min, *J. Nanopart. Res.*, 2018, **20**, 310.

42 W. Wang, H. Zhang, S. Zhang, Y. Liu, G. Wang, C. Sun and H. Zhao, *Angew. Chem., Int. Ed.*, 2019, **58**, 16644–16650.

43 M. Hassan, Y. Slimani, M. A. Gondal, M. J. S. Mohamed, S. Güner, M. A. Almessiere, A. M. Surrati, A. Baykal, S. Trukhanov and A. Trukhanov, *Ceram. Int.*, 2022, **48**, 24866–24876.

44 T. Yang, Y. Tang, F. Yang, J. Qu, X. Yang, Y. Cai, F. Du, C. M. Li and J. Hu, *Chem. Eng. J.*, 2023, **475**, 146497.

45 K. Nabil, N. Abdelmonem, M. Nogami and I. Ismail, *Materials*, 2020, **13**, 655.

46 B. Padmaja, S. Dhanapandian and K. Ashokkumar, *J. Mater. Sci. Eng. B*, 2023, **297**, 116699.

47 X. Wei, X. Wang, Y. Pu, A. Liu, C. Chen, W. Zou, Y. Zheng, J. Huang, Y. Zhang, Y. Yang, M. Naushad, B. Gao and L. Dong, *Chem. Eng. J.*, 2021, **420**, 127719.

48 H. Chai, C. Yang, P. Xu, P. Wang, J. Qu and G. Zhang, *J. Clean. Prod.*, 2022, **377**, 134511.

49 G. Palanisamy, N. H. Al-Shaalan, K. Bhuvaneswari, G. Bharathi, G. Bharath, T. Pazhanivel, V. E. Sathishkumar, M. K. Arumugam, S. K. K. Pasha, M. A. Habila and A. El-Marghany, *Environ. Res.*, 2021, **201**, 111429.

50 D. Pradhan, L. Mohanty, R. Singhal, E. Falletta and S. K. Dash, *Inorg. Chem. Commun.*, 2023, **156**, 111259.

51 T. D. Munusamy, C. S. Yee and M. M. R. Khan, *Adv. Powder Technol.*, 2020, **31**, 2921–2931.

52 Z. Bezu, A. M. Taddesse and I. Diaz, *J. Photochem. Photobiol., A*, 2024, **449**, 115369.

53 A. Toghan and A. Modwi, *J. Photochem. Photobiol., A*, 2021, **419**, 113467.

54 S. Senobari and A. Nezamzadeh-Ejhieh, *J. Mol. Liq.*, 2018, **257**, 173–183.

55 S. Guo, G. Zhang and J. Wang, *J. Colloid Interface Sci.*, 2014, **433**, 1–8.

56 B. Palanivel, M. Lallimathi, B. Arjunkumar, M. Shkir, T. Alshahrani, K. S. Al-Namshah, M. S. Hamdy, S. Shanavas, M. Venkatachalam and G. Ramalingam, *J. Environ. Chem. Eng.*, 2021, **9**, 104698.

57 L. Li, J. Gao, Y. Yuan, S. Zhang, M. Liang and Y. Liu, *J. Taiwan Inst. Chem. Eng.*, 2021, **126**, 134–144.

58 Y. Yao, G. Wu, F. Lu, S. Wang, Y. Hu, J. Zhang, W. Huang and F. Wei, *Environ. Sci. Pollut. Res.*, 2016, **23**, 21833–21845.

59 T. Wang, J. Zheng, J. Cai, Q. Liu and X. Zhang, *Sci. Total Environ.*, 2022, **839**, 155955.

60 T. T. T. Nguyen, Y. N. N. Nguyen, X. T. Tran, T. T. T. Nguyen and T. V. Tran, *J. Environ. Chem. Eng.*, 2023, **11**, 111003.

61 R. G. Pearson, *Inorg. Chem.*, 1988, **27**, 734–740.

62 M. Moradi, F. Hasanvandian, A. A. Isari, F. Hayati, B. Kakavandi and S. R. Setayesh, *Appl. Catal., B*, 2021, **285**, 119838.

63 W. Zhang, S. Zhao, Y. Xing, H. Qin, Q. Zheng, P. Zhang, S. Zhang and X. Xu, *Chem. Eng. J.*, 2022, **442**, 136151.

64 S. Taghilou, M. R. Mehrasbi, A. Esrafili, E. Dehghanifard, M. Kermani, B. Kakavandi and S. Giannakis, *J. Mater. Chem. A*, 2024, **12**(30), 19532–19550.

65 N. Q. Man, N. T. V. Hoan, N. T. Vinh, L. Van Thanh Son, V. T. Nguyen, P. T. K. Thu, N. Van Hung, L. T. Hieu and D. Q. Khieu, *J. Mater. Sci. Mater. Electron.*, 2024, **35**, 114.

66 B. El Allaoui, H. Benzeid, N. Zari, A. l. Kacem Qaiss and R. Bouhfid, *Int. J. Biol. Macromol.*, 2024, **259**, 128893.

67 B.-E. Channab, M. E. Ouardi, S. E. Marrane, O. A. Layachi, A. E. Idrissi, S. Farsad, D. Mazkad, A. BaQais, M. Lasri and H. A. Ahsaine, *RSC Adv.*, 2023, **13**, 20150–20163.

68 K. H. Nasir and H. A. Alshamsi, *J. Inorg. Organomet. Polym. Mater.*, DOI: **10.1007/s10904-024-03266-2**.

69 N. A. Jasim, S. E. Ebrahim and S. H. Ammar, *Results Opt.*, 2023, **13**, 100508.

70 D. Ma, J. Tang, G. He, Y. Xue, S. Pan, F. Liu and J. Zhao, *Mater. Sci. Semicond. Process.*, 2024, **181**, 108672.

71 M. Terki, S. Triaa, F. K. Ali, R. Youcef, I. O. Brahim and M. Trari, *React. Kinet. Mech. Catal.*, 2023, **136**, 1143–1155.

72 M. Saeed, M. Siddique, M. Ibrahim, N. Akram, M. Usman, M. A. Aleem and A. Baig, *Environ. Prog. Sustain. Energy*, 2020, **39**, e13408.